† Electronic supplementary information (ESI)

Combining negative photoconductivity and resistive switching towards in-memory logic operations†

Subham Paramanik[1] and Amlan J. Pal[1,2,*]

[1]School of Physical Sciences, Indian Association for the Cultivation of Science, Jadavpur, Kolkata 700032, India
[2]UGC-DAE Consortium for Scientific Research, University Campus, Khandwa Road, Indore 452001, India

Characteristics of the Thin Films

The optical absorption spectra of the thin films are shown in Fig. S1a. They exhibit a high absorption value throughout the visible region with a clear onset at around 700 nm which matches the reported results.[S1] The optical bandgap of the compounds could be estimated from the corresponding Tauc plots (Fig. S1b). The bandgap was 1.8 eV and did not vary in the series of the rudorffites. The additional peak in the low wavelength region (~400 nm) appearing in the silver-rich rudorffite occurs due to unreacted AgI in the films.

To study the phase purity of the compounds, X-ray diffraction (XRD) patterns of the rudorffites was recorded (Fig. S1c). The silver- and bismuth-rich compounds are known to crystallize in rhombohedral (R-3m space group) and cubic-spinel structure (Fd-3m space group), respectively.[S2,S3] The equimolar compound ($AgBiI_4$) can crystallize in either of the aforementioned structures. The patterns presented in Fig. S1c show that the crystal structure of $Ag_mBi_nI_{m+3n}$ was dependent of the relative amounts of silver and bismuth in the precursors. The XRD patterns of the balanced ($AgBiI_4$) and the silver-rich (Ag_2BiI_5) compounds show two signature peaks of (110) and (108) planes at around 42° signifying the occurrence of the rhombohedral phase having R-3m symmetry and are in well agreement with the reported results.[S2] The bismuth-rich compound, on the other hand, exhibited a clear signature peak of (440) plane at ~42° (Fig. S1d) implying a highly crystalline cubic structure with Fd-3m space group symmetry. The presence of some impurity peaks (marked with *) has also been observed ($2\theta = 22.5°$) for the Ag_2BiI_5 compound; such peaks reflect the presence of unreacted AgI in the material (Fig. S1e). Moreover, repetition of (003) and (111) planes support the overall high crystallinity and preferred orientation of the material.[S4]

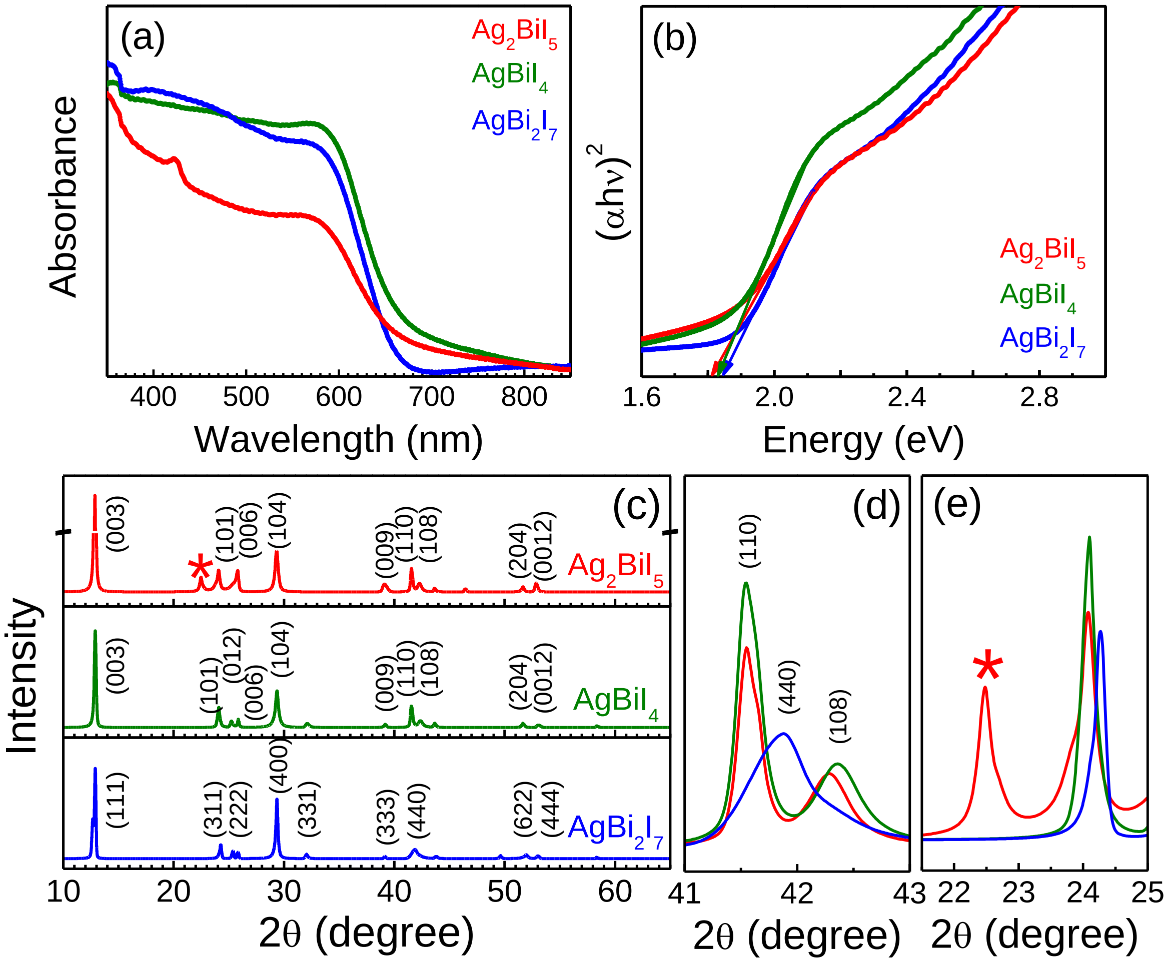

Fig. S1 (a) Optical absorption spectra, (b) corresponding Tauc plots, (c) XRD patterns, and patterns in a small range of (d) 41° to 43° and (e) 22° to 25° (showing the signature peak of the unreacted AgI with an asterisk) of different ruddorfites.

We also probed the surface morphologies of the films through field emission scanning electron microscopy (FESEM) and atomic force microscopy (AFM) in a noncontact mode. The FESEM measurements were associated with energy dispersive X-ray (EDX) composition analysis, which confirmed the formation of the compounds in their phase-pure forms (Fig. S2). The FESEM and AFM images show that the films were compact and homogeneous in nature. The AFM topographies of an intentional scratch and their corresponding line profiles provided the thickness of the thin films (Fig. S3). The calculated film thickness was 140 nm with a RMS roughness of 20 nm. Devices were hence fabricated based on films having an identical thickness.

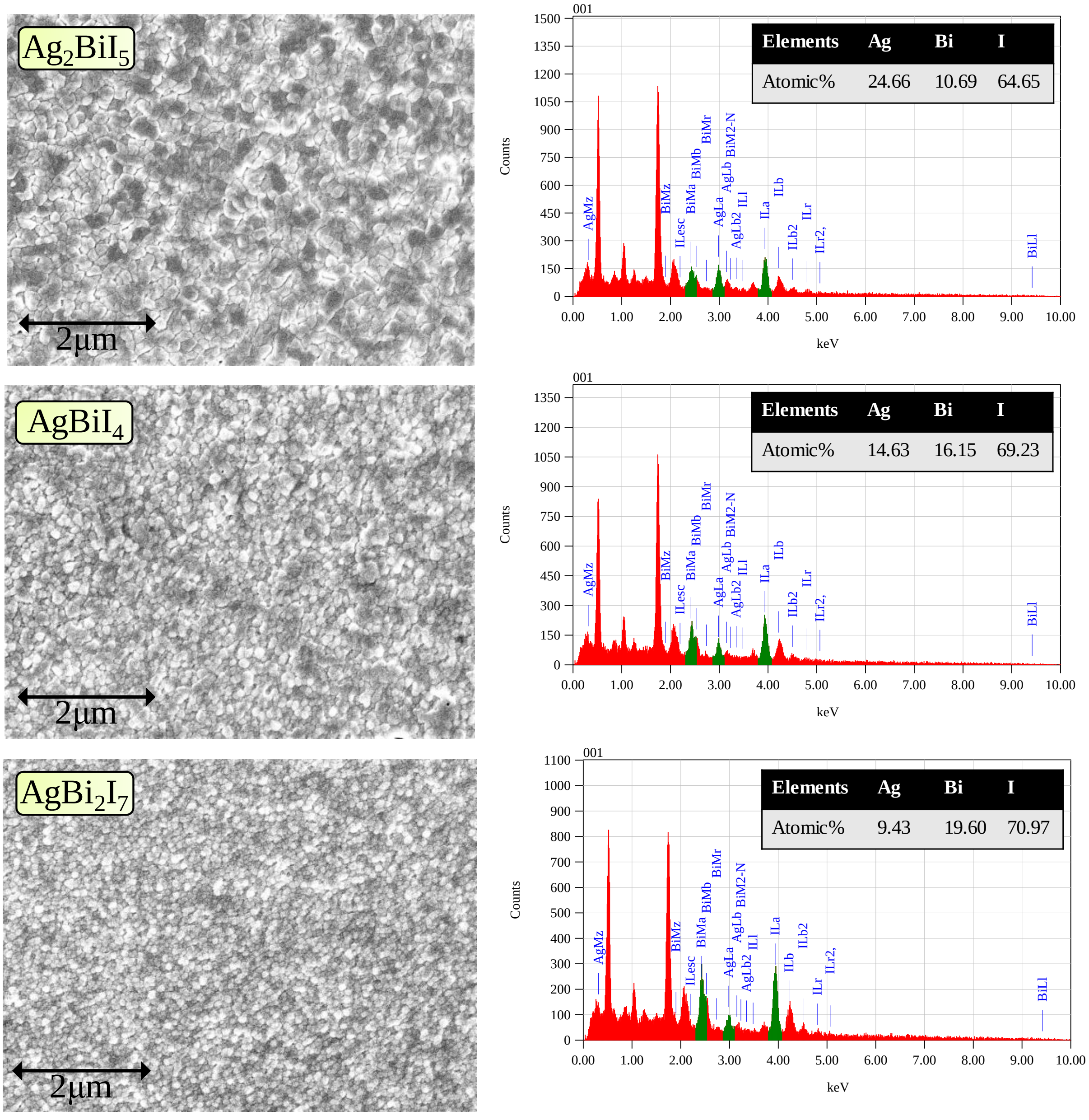

Elements	Ag	Bi	I
Atomic%	24.66	10.69	64.65

Elements	Ag	Bi	I
Atomic%	14.63	16.15	69.23

Elements	Ag	Bi	I
Atomic%	9.43	19.60	70.97

Fig. S2 FESEM images and the corresponding EDX spectra of different ruddorfites in their thin-film form.

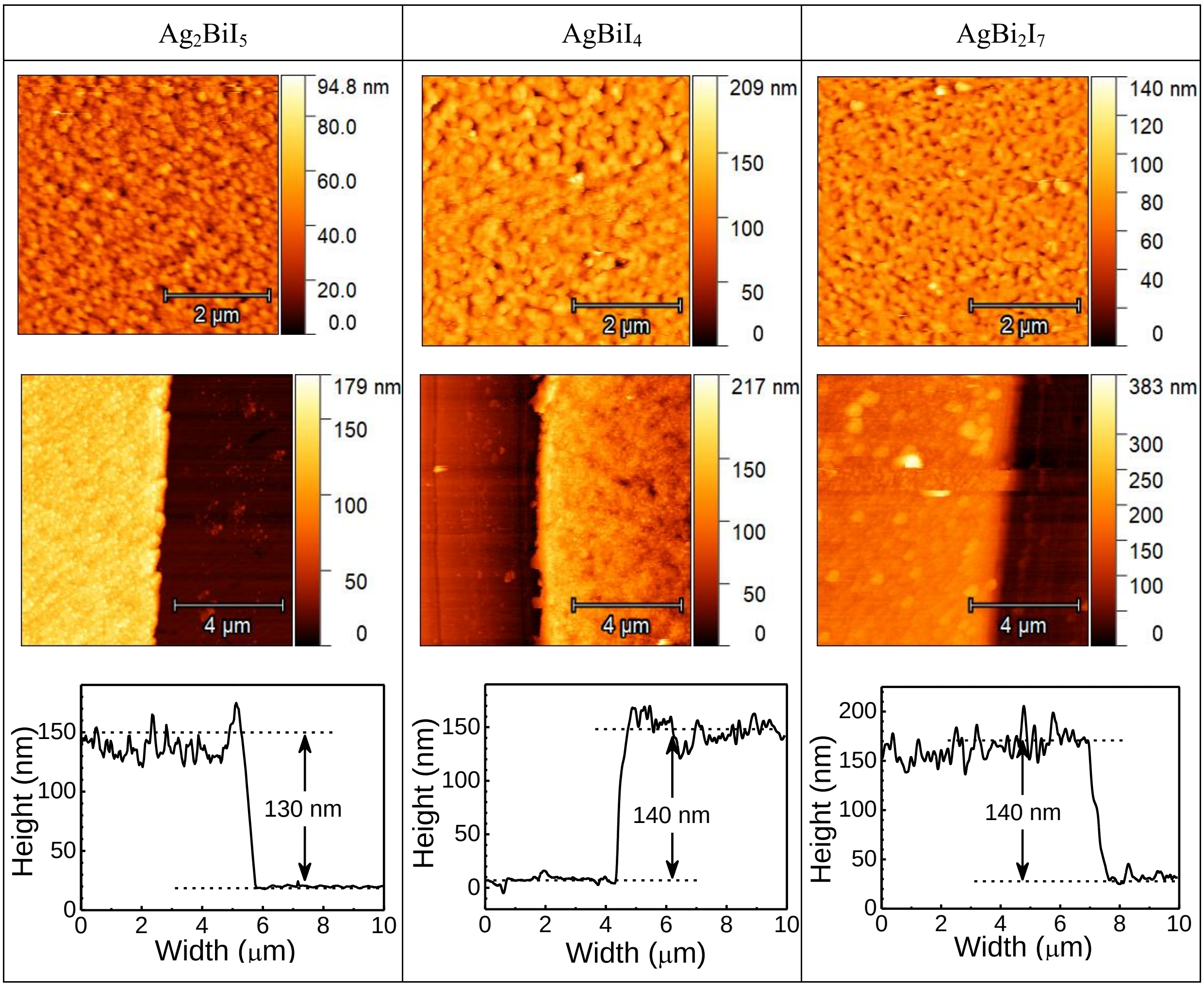

Fig. S3 AFM topographies of different ruddorfites in their pristine thin films and with an intentional scratch and the corresponding line profiles in calculating the film thicknesses.

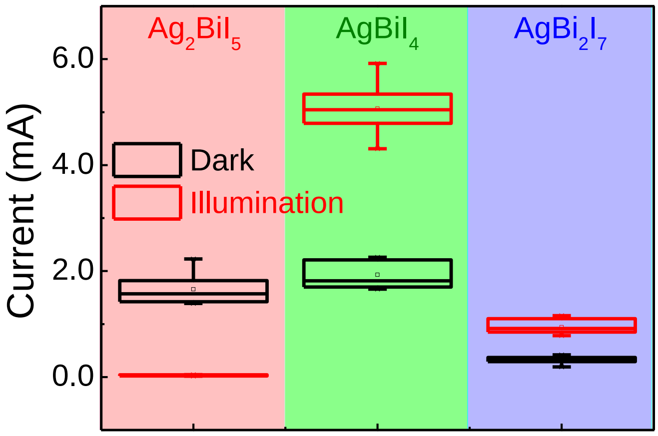

Fig. S4 The box-chart plots of current at 0.7 V under dark and illumination conditions for devices based on the three compounds.

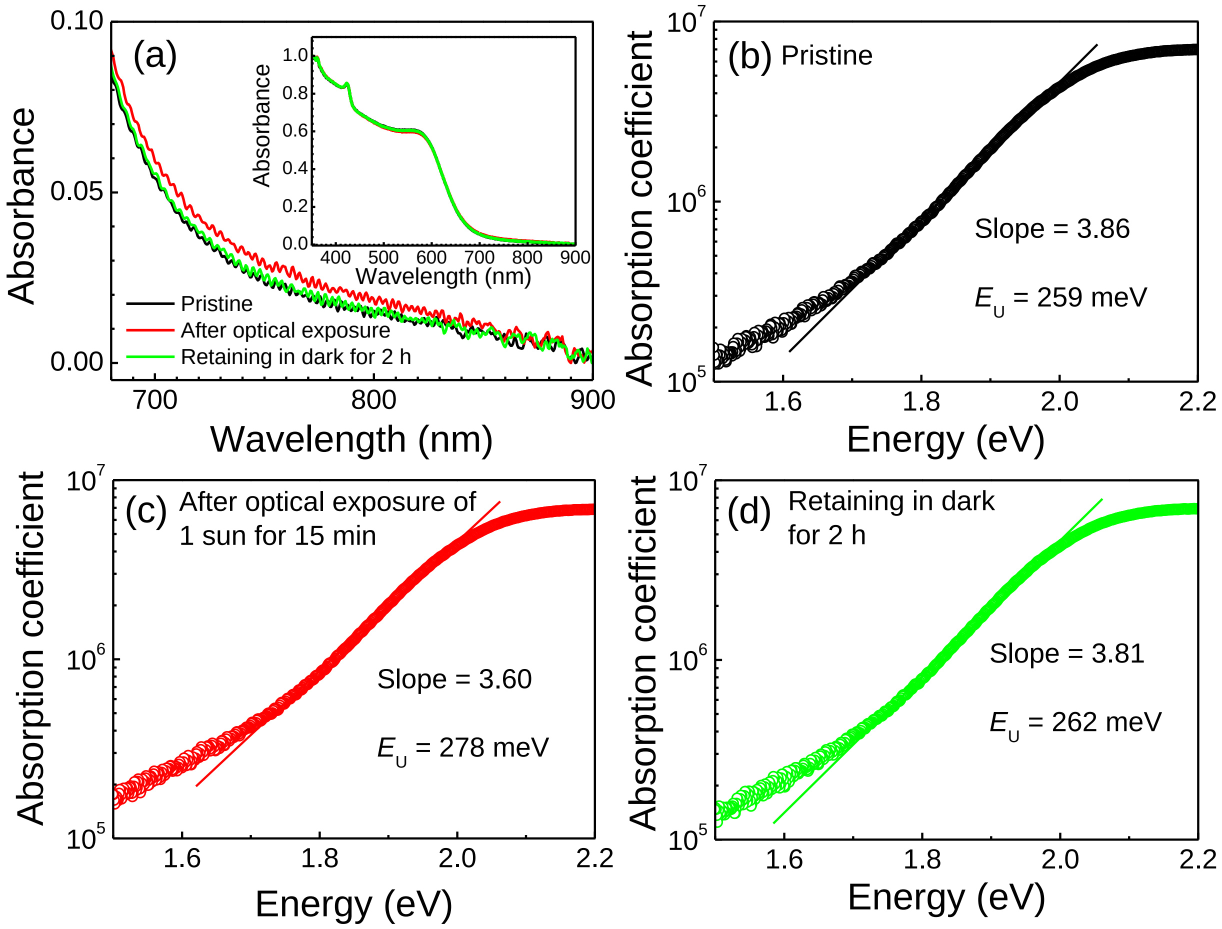

Fig. S5 (a) Optical absorption spectra of an Ag_2BiI_5-based thin film measured just after fabrication, keeping under 1 sun illumination for 15 min, and then retaining the same film under dark for 2 h. Inset of (a) shows the full range spectra of the films. (b) - (d) Urbach energy calculation under the three conditions as mentioned in the legend.

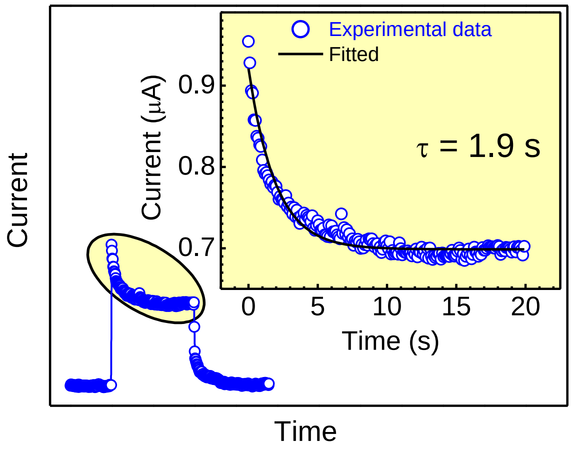

Fig. S6 Decay characteristics of the photocurrent under illumination for an $AgBi_2I_7$-based device while attaining a stable PPC state.

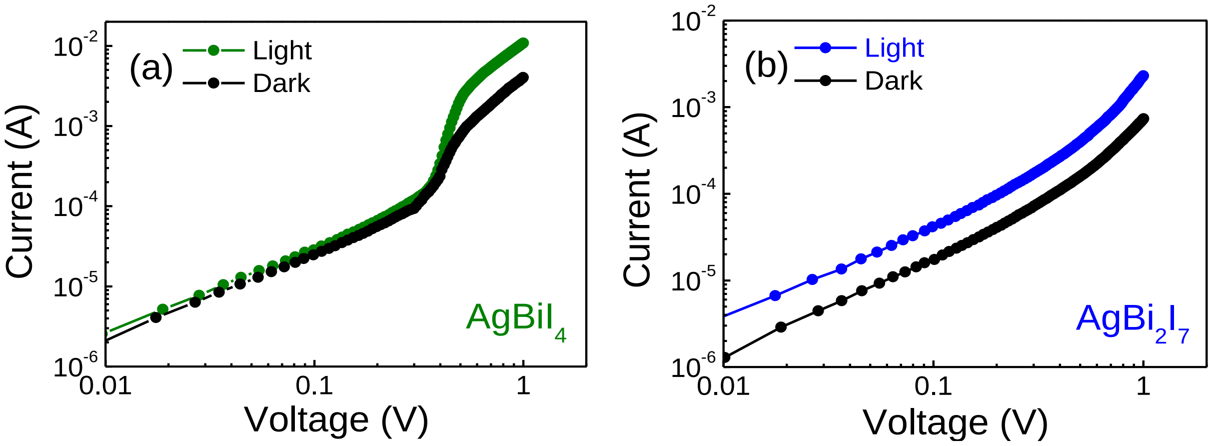

Fig. S7 Current-voltage characteristics of the (a) $AgBiI_4$ and (b) $AgBi_2I_7$-based devices in a double-logarithmic scale.

Discussion regarding the conduction mechanism: In general, devices based on many halide perovskite show the resistive switching by the formation and rupture of the conducting filaments under the application different bias polarity. For the present devices, the resistive switching can be explained by the interfacial type switching where the whole process is dominated the trapping and detrapping of the charge carriers in the interfacial defect states. Fig. S7 shows the *I*-*V* characteristics of the devices in double logarithmic scale in different bias regions. In the low positive voltage (Fig. S7a), the *I*-*V* characteristics follow Ohmic behavior (slope = 1.1). When the voltage reaches to a threshold value (V_{Set}) and thereby injects carriers to fill the trap states, the trap-filling process prompt the modulation of the Schottky barrier at the interface and the current start to increase sharply. In such a condition, the space-charge limited conduction process, as governed by the Child's law (slope = 2), becomes dominant. As all the trap-states are filled by the injected carriers, the perovskite can be considered as trap-free with a reduced barrier high across the junction. During the ramping down of the voltage, due to the filled trap-states, the LRS prevails until a suitable bias of opposite polarity could detrap the carriers in restoring the barrier height. After the electrical erase process, the current in the high field region shows a slope of 1.5 (Fig, S7b). To describe this region, the device current has been plotted with respect to $V^{1/2}$ (Fig. S7c); the linear dependence of the plot supports thermionic emission as the conduction mechanism. Finally, with further decreasing the bias, the device finally enter into the Ohmic region again.

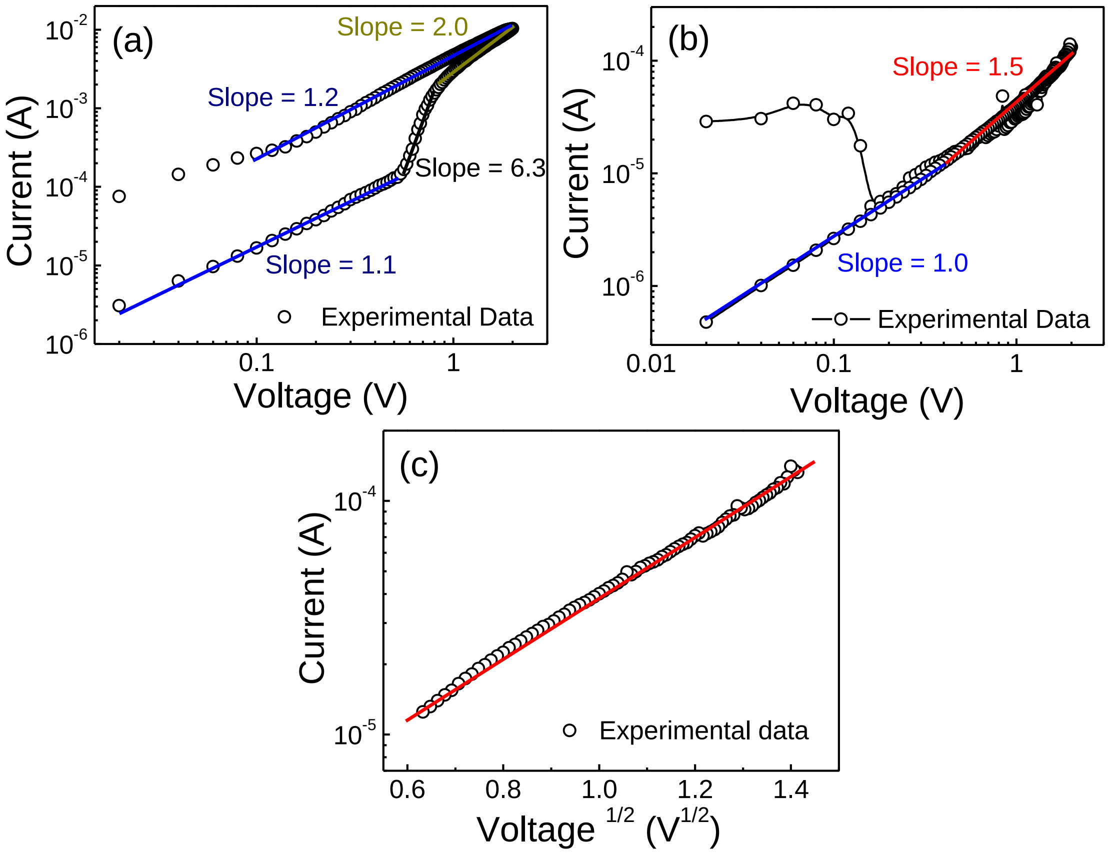

Fig. S8 (a) and (b) represent the current versus voltage characteristics of the devices in double logarithmic scale for the positive and negative bias regions, respectively. (c) The current versus $V^{1/2}$ plot in the negative voltage region after the reset process.

Table S1. A comparison of the set and the reset voltages of the devices with different reports.

Device Structure	Set voltage (V)	Reset voltage (V)	Year	Reference
ITO/PEDOT:PSS/Cs_4PbBr_6/Au	0.5 to 2	-0.6	2019	S5
ITO/$MAPbI_{3-x}Cl_x$/$(BA)_2MA_{n-1}Pb_nX_{3n-1}$/Al	0.79	-0.77	2020	S6
ITO/$MA_3Bi_2I_9$/Cu	1	-6.4	2021	S7
ITO/$Cs_3Bi_2Br_9$/Al	-0.45	2.2	2022	S8
ITO-PET/$CsPb_2Br_5$/Al	2.34	-2.04	2022	S9
ITO/Cu_3SbI_6/ PMMA/Ag	0.71	-0.71	2022	S10
ITO/Ag_3SbI_6/ PMMA/Ag	1.0	1.15	2022	S10
ITO/Ag_2BiI_5/PMMA/Al	**0.58**	**0.25**	**-**	**This Work**

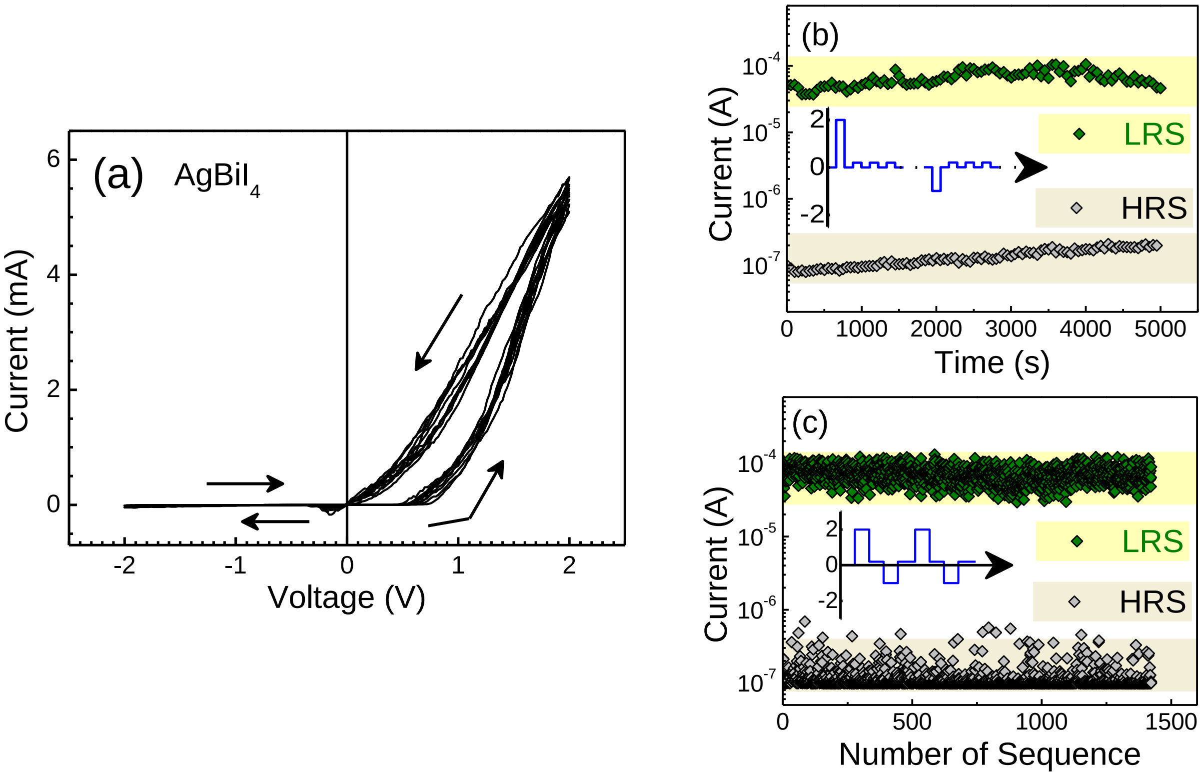

Fig. S9 (a) Current-voltage characteristics of a device based on $AgBiI_4$ under application of a voltage in multiple loops under dark condition. (b) Current output of the LRS and HRS under a train of 0.2 V voltage pulse to study the WORM application. (c) Current output of the LRS and HRS under a 0.2 V voltage pulse when the two states were flipped in sequence to study the RAM application. In (b) and (c), the LRS and HRS were induced by applying +2.0 and -1.0 V, respectively; the scheme of voltage pulse used in the measurements is shown in the inset of the respective figures.

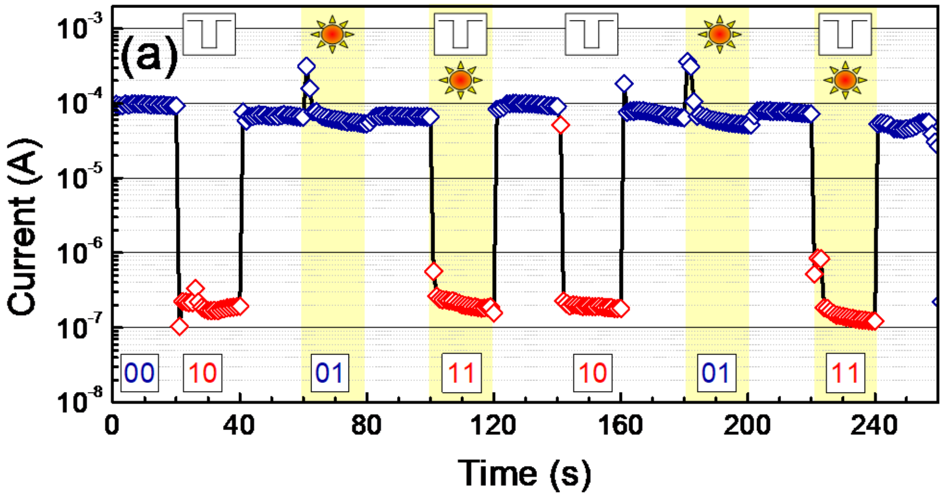

(b) Input Signal		Output	
Electrical	Optical	Resistance	State
0	0	Low	0
1	0	High	1
0	1	Low	0
1	1	High	1

Fig. S10 (a) Device current under a train of +0.2 V pulse after different combinations of independent electrical and optical inputs were imposed to an $AgBiI_4$-based device. (b) Device resistance as the output under the application of the two inputs in four combinations as a truth table.

References

S1 I. Turkevych, S. Kazaoui, E. Ito, T. Urano, K. Yamada, H. Tomiyasu, H. Yamagishi, M. Kondo and S. Aramaki, *ChemSusChem*, 2017, **10**, 3754-3759.

S2 Z. W. Xiao, W. W. Meng, D. B. Mitzi and Y. F. Yan, *J. Phys. Chem. Lett.*, 2016, **7**, 3903-3907.

S3 A. Bera, S. Paramanik, A. Maiti and A. J. Pal, *Phys. Rev. Mater.*, 2021, **5**, 095404.

S4 A. Chakraborty, N. Pai, J. Zhao, B. R. Tuttle, A. N. Simonov and V. Pecunia, *Adv. Funct. Mater.*, 2022, **32**, 2203300.

S5 R. Q. Chen, J. Xu, M. M. Lao, Z. W. Liang, Y. K. Chen, C. J. Zhong, L. J. Huang, A. Z. Hao and M. Ismail, *Phys. Status Solidi-Rapid Res. Lett.*, 2019, **13**, 1900397.

S6 F. Xia, Y. Xu, B. X. Li, W. Hui, S. Y. Zhang, L. Zhu, Y. D. Xia, Y. H. Chen and W. Huang, *ACS Appl. Mater. Interfaces*, 2020, **12**, 15439-15445.

S7 S. Poddar, Y. T. Zhang, Y. Y. Zhu, Q. P. Zhang and Z. Y. Fan, *Nanoscale*, 2021, **13**, 6184-6191.

S8 X. Cao, Z. Ma, T. Cheng, Y. Wang, Z. Shi, J. Wang and L. Zhang, *Energy Environ. Mater.* , 2022, 10.1002/eem1002.12419.

S9 T. Paul, P. K. Sarkar, S. Maiti, A. Sahoo and K. K. Chattopadhyay, *Dalton Trans.*, 2022, **51**, 3864-3874.

S10 Y. M. Yuan, Y. C. Wang, X. S. Tang, N. Zhang and W. X. Zhang, *ACS Appl. Mater. Interfaces*, 2022, **14**, 53990-53998.